RSC Advances

PAPER

View Article Online
View Journal | View Issue

Cite this: *RSC Adv.*, 2015, **5**, 33878

Zn^{2+} mediated solvent free solid state red emitting fluorescent complex formation in a mortar–pestle along with living cell imaging studies†

Susanta Adhikari,*[a] Avijit Ghosh,[a] Sandip Mandal,[b] Animesh Sahana[b] and Debasis Das[b]

Received 19th January 2015
Accepted 30th March 2015

DOI: 10.1039/c5ra01059d

www.rsc.org/advances

An acridone based highly Zn^{2+} selective, cell-permeable turn-on fluorescence probe (**AAS**) shows yellow fluorescence at 560 nm (λ_{ex}, 445 nm) in dry methanol/DMSO up to 100 μM Zn^{2+}. At higher Zn^{2+} concentration (>100 μM in dry methanol) **AAS** yields a red solid polymeric complex having strong emission at 605 nm. Interestingly, the red solid polymer also appears at relatively lower Zn^{2+} concentration (>50 μM) in water. The lowest detection limit of **AAS** is 0.1 nM Zn^{2+}. **AAS** is employed for fluorescence bio-imaging of Zn^{2+} in human MCF 7 breast cancer cells and *HeLa* cells. Moreover, AAS develops an orange colour detectable by the naked eye in the presence of trace Zn^{2+} in a mixture of various common cations and anions in the solid state (requires no solvent). Hence, this method is extremely green and interference free. AAS can be employed as a laboratory indicator for detection of Zn^{2+} in real samples and live cells.

1. Introduction

Zinc plays an important role in cell growth,[1] apoptosis and metabolism,[2] gene expression, signal transduction,[3,4] regulation of endocrine,[5] and immune and neuronal functions implicated in the pathophysiology of depression.[6] Severe Zn deficiencies cause developmental anomalies in human and animals while an increased Zn level causes high cytotoxicity in the context of acute brain injury.[7] The role of Zn^{2+} in prostate cancer cells, ER-positive MCF-7 breast cancer cells, human melanoma cells and many other important biological processes demands its accurate trace level measurement in biological systems. Evidence for a zinc uptake transporter in human prostate cancer cells has already been established.[8] Expression of the zinc transporter ZnT4 decreases in the progression from early prostate disease to invasive prostate cancer.[9] In the prostate, zinc is believed to help with reproductive functions by aiding in the accumulation of citrate, a component of semen and has a protective role against development and progression of prostate cancer.[10,11] However, recent observations indicate that high supplemental zinc intake is associated with an increased risk of advanced prostate cancer (PCa).[11–14] Tamoxifen, a non-steroidal, selective estrogen receptor modulator (SERM) has been used as an antagonist for treatment of estrogen receptor (ER)-positive breast cancer. It has been found that Zn^{2+} mediates tamoxifen-induced autophagy and cell death in MCF-7 breast cancer cell line.[15] Several probes can monitor low mobile Zn^{2+} concentration for *in vivo* testing *via* living cell-imaging.[16,17] As Zn^{2+} concentration varies with physiological environments, *viz.* 12 μM in serum and 0.1–0.5 μM in gray matter and the brain, the development of a nontoxic interference free Zn^{2+} sensor with concentration tunable emission properties is highly demanded. Visible light excitation minimizes photo damage and background interference from auto-fluorescence of biological samples.[18,19] Zn^{2+} sensors are primarily based on fluorescein, coumarin, di-picolyl amine *etc.*[20–25] Substituted benzoxazole derivative sensing Zn^{2+} *via* excited-state intramolecular proton transfer (ESIPT) is also reported.[26] Acridone alkaloids having varieties of biological activities *viz.* anticancer, antimicrobial, antiviral and anti-parasitic properties[27] have been used for labelling and fluorescence-based assays for their chemical inertness and resistance to photo-bleaching. Acridones can also detect bio-molecules and, are used to measure Lewis acidity of cations[28] and monitoring of enzyme activity.[29] Recently, we have reported heme-interacting acridone derivative that can prevent free heme-mediated protein oxidation and degradation, markers for heme-induced oxidative stress.[27] In contrast to fluorescein, dansyl, anthracene and rhodamine moieties, mostly used in chemosensors, acridone is highly resistant to photo-bleaching. Our ongoing effort for improved sensors[16,30] have resulted a new acridone derivative, (*E*)-4-(2-hydroxybenzylideneamino)acridin-9(10*H*)-one (**AAS**) for selective sensing of Zn^{2+} under solvent free condition. To the best of our knowledge, this is the first report on visible light

[a]*Department of Chemistry, University of Calcutta, 92, A.P.C. Road, Kolkata 700 009, West Bengal, India. E-mail: adhikarisusanta@yahoo.com; Fax: +91 33 23519755; Tel: +91 33 23509937*

[b]*Department of Chemistry, The University of Burdwan, Burdwan 713104, West Bengal, India*

† Electronic supplementary information (ESI) available. See DOI: 10.1039/c5ra01059d

excitable, Zn^{2+} assisted polymeric complex formation which gives intense solid state red emission (orange in naked eye) of **AAS**. Naked eye detection of a colorless d^{10} cation (Zn^{2+}) under solvent free and interference free condition is a significant and challenging contribution to green chemistry. Cd^{2+} interferes in dry test for Zn^{2+} detection in solid state.[31] Visible light excitation and strong red emission are highly desirable *in vivo* application. We have been successful to cluster all the desired properties in a single probe, **AAS**. Moreover, **AAS–Zn^{2+}** system having solid state red fluorescence may be useful in optoelectronic applications.

2. Experimental section

2.1 General information of materials and methods

All metal cation were used as either their nitrate or their chloride salts and the anions as their Na salts. Other chemicals were of analytical reagent grade and used without further purification except when specified. Milli-Q Milipore 18.2 MΩ cm^{-1} water was used throughout all experiments. A JASCO (model V-570) UV-vis spectrophotometer was used for recording UV-vis spectra. FTIR spectra were recorded on a JASCO FTIR spectrophotometer (model FTIR-H_2O). Mass spectra were carried out using a QTOF Micro YA 263 mass spectrometer in ES positive mode. ^{1}H NMR spectra were recorded using a Bruker Avance 300 (300 MHz) inDMSO-d_6 whereas ^{13}C NMR spectra were recorded using a Bruker Avance 500 (125 MHz) in DMSO-d_6. Melting point was measured with a VEEGO digital melting point apparatus. Elemental analysis was performed using a Perkin-Elmer CHN-Analyzer with the first 2000-Analysis kit. Steady-state fluorescence emission and excitation spectra were recorded with a Hitachi-Hitachi F-4500 spectrofluorometer. A Systronics digital pH meter (model 335) was used to measure the solution pH. Either 50 mM HCl or KOH was used for pH adjustment.

2.2 Synthesis of ligand AAS

Scheme 1 presents the synthetic protocol of **AAS**. 4-Amino acridone, the signalling unit is synthesized following our published procedure.[27] The acridone based ligand **AAS** can be synthesised by the Schiff's base formation between 4-amino acridone (**2**) with salicylaldehyde.

320 mg of **2** (1.508 mmol) and 0.116 mL of salicylaldehyde (1.508 mmol) were taken in 10 mL of dry methanol and refluxed under argon for 6 h. A yellow solid precipitate was obtained. Filtered the solid and washed with cold methanol, dried in vacuum to obtain 375 mg (yield ~ 80%) of **AAS** as a yellow solid. ^{1}H NMR (Fig. S1†) (300 MHz, DMSO-d_6): δ 6.97 (d, 2H, J = 8.1 Hz, d), 7.23 (m, 2H, e), 7.44 (m, 1H, f), 7.53 (d, 1H, J = 7.5 Hz, g), 7.69 (m, 1H, h), 7.89 (d, 2H, J = 8.1 Hz, i), 8.11 (d, 1H, J = 9.9 Hz, j), 8.19 (d, 1H, J = 8.1 Hz, k), 8.98 (s, 1H, c), 10.87 (s, 1H, b), 11.53 (s, 1H, a); ^{13}C NMR (Fig. S2†) (125 MHz, DMSO-d_6) δ 118.96, 121.36, 122.59, 123.85, 124.44, 126.09, 126.52, 127.43, 128.35, 129.31, 131.22, 137.30, 138.69, 139.13, 140.65, 144.73, 146.15, 164.91, 168.56, 182.07; HRMS (Fig. S3†), m/z $(M + H)^+$ calculated for $C_{20}H_{14}N_2O_2$: 315.3453, found: 315.3453. IR (neat) λ_{max} 3392.78, 1598.98, 1521.83, 1452.39, 1332.81, 1274.94, 744.52 (Fig. S4†).

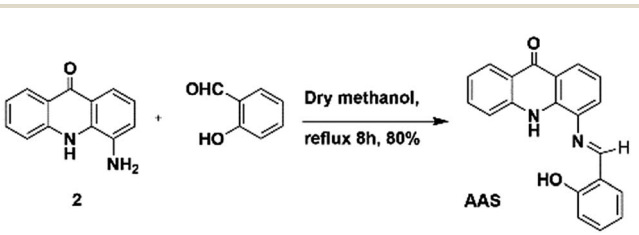

Scheme 1 Synthetic protocol of AAS.

2.3 Synthesis of 2-(2-aminophenylamino)benzoic acid (1)

A mixture of 1,2-phenylenediamine (2 g, 18.50 mmol), 2-chloro benzoic acid (2.89 g, 13.08 mmol), powdered Cu (200 mg), Cu_2O (200 mg), trans 1,2-cyclohexyldiamine (10 mol%) and K_2CO_3 (3.873 g, 27.75 mmol) in diglyme (30 mL) were heated under reflux for 8 h. Excess diglyme was removed by distillation and the mixture poured into 1 L of hot water. Then 10 mL of 6(N) HCl was added to the mixture. The bluish black solid formed was filtered, washed and collected. The crude acid was dissolved in aqueous KOH, boiled in presence of activated charcoal and filtered. On acidification of the filtrate with HCl, a bluish black solid precipitate of **1** was obtained 1.26 g (yield ~ 30%). R_f: 0.41 (2% methanol in dichloromethane); mp: 125–127 °C; ^{1}H NMR (Fig. S5†) (300 MHz, DMSO-d_6) δ 6.67 (m, 1H), 6.76 (m, 1H), 7.19 (d, 2H, J = 7.2 Hz), 7.32 (d, 2H, J = 7.2 Hz), 7.39 (d, 1H, J = 6.9 Hz), 7.89 (d, 1H, J = 6.6 Hz), 9.18 (s, 1H); HRMS (Fig. S6†) m/z $(M + H)^+$ calculated for $C_{13}H_{12}N_2O_2N$: 229.2545, found: 229.2543.

2.4 Synthesis of 4-amino acridone (2)

400 mg (1.75 mmol) of **1** was taken in a round bottom flask to which 5 mL of Eaton's reagent was added. The mixture was heated under stirring condition in nitrogen atmosphere for 2 h, whereby the mixture turned to yellow colour. Then the reaction mixture was poured into 500 mL cold water and made alkaline by liquor ammonia. The greenish yellow precipitate formed was filtered, washed with water and dried. The crude solid was purified by silica gel column chromatography using 15% MeOH in dichloromethane as eluent to obtain **2** (238 mg, yield ~ 65%) as light green solid. R_f: 0.3 (10% methanol in dichloromethane); mp: 300 °C; IR (neat) ν_{max} 3410.26, 1680.05, 1506.46, 1452.45, 1230.63, 1128.39; ^{1}H NMR (Fig. S7†) (300 MHz, DMSO-d_6) δ 6.90 (m, 2H), 7.10 (m, 1H), 7.40 (m, 1H), 7.60 (m, 2H), 8.11 (dd, 1H, J = 8.25, 1.05 Hz), 10.522 (bs, 1H); HRMS (Fig. S8†) m/z $(M + H)^+$ calculated for $C_{13}H_{10}N_2O$: 211.2393, found: 211.2365.

An alternative route for compound **1** following two steps reaction sequences *via* 2-((2-nitrophenyl)amino)benzoic acid (**1A**) was also adopted (Scheme S1, ESI†). In this route, 2-nitroaniline was condensed with 2-chlorobenzoic acid using Ullmann reaction to obtain **1A** and subsequent reduction of the nitro group in presence of $SnCl_2$ in methanol resulted compound **1** in good yields. ^{1}H NMR, ^{13}C NMR, TOF-MS and ATIR (Fig. S1–10†) are used for its structure elucidation (Scheme 2).

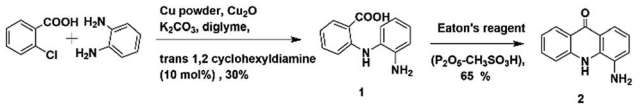

Scheme 2 Synthetic route of 4-amino acridone (**2**).

3. Results and discussion

3.1 Effects of Zn^{2+} on spectroscopic properties of AAS

Emission properties of **AAS** have been observed in HEPES buffered aqueous methanol (0.1 M, water–methanol, 97.5 : 2.5, v/v, pH 7.4). The pattern is almost same to that of dry methanol; however emission intensities and wavelengths are slightly different (Fig. S20, ESI†). In presence of Zn^{2+}, the emission band of **AAS** is red shifted in MeOH, DMSO and mixed solvents (water–methanol/DMSO, 97.5 : 2.5, v/v). In dry methanol, the red shift is about 18 nm (**AAS**: λ_{em}, 542 nm; **AAS–Zn^{2+}** adduct: λ_{em}, 560 nm). Additionally, at higher Zn^{2+} concentration, **AAS** forms a red precipitate in dry methanol which shows solid state red fluorescence (λ_{em}, 605 nm). The red polymer gradually forms upon addition of water in methanol solution of the **Zn^{2+}–AAS** adduct. Solvent and pH, two influential parameters have been optimized to study the photo-physical properties of **AAS** and its Zn^{2+} adduct shows the emission intensities of the systems is highly solvent dependent (Fig. S11, ESI†). Interestingly, emission intensity of free **AAS** increases with increasing water content up to ~35% (v/v) followed by gradual decrease to the minimum at 97.5% (v/v, λ_{ex} = 445 nm, Fig. S12, ESI†). On the other hand, emission intensity of **AAS–Zn^{2+}** system decreases gradually with increasing water percentage (Fig. S13, ESI†). However, **AAS–Zn^{2+}** system have always higher emission intensity than free **AAS**. Fluorescence titrations have been performed both in dry and aqueous methanol (97.5 : 2.5, v/v) to have deeper insight of role of water on **AAS–Zn^{2+}** interaction. Changes in the fluorescence spectra of **AAS** upon addition of Zn^{2+} in dry methanol are presented in Fig. 1. Lowest detection limit of **AAS** is 0.0001 μM of Zn^{2+}. The emission intensities gradually increase with increasing Zn^{2+} (Fig. S18, ESI†), the linear region of the plot, (inset, Fig. S18, ESI†) is useful for determination of unknown Zn^{2+} concentration. In presence of Zn^{2+}, emission intensity of free **AAS** enhances ~41.36 fold in dry methanol whereas in 97.5% water–methanol (v/v), enhancement is ~8.42 fold. Fig. S19 (ESI†) shows the colour changes of **AAS** upon gradual addition of Zn^{2+} in dry methanol whereas Fig. S21 (ESI†) shows the colour changes of **AAS** in presence of Zn^{2+} in HEPES buffered media under hand held UV lamp. Here, the linearity is observed up to 10 μM Zn^{2+} (Fig. S22, ESI†).

The absorbance of free **AAS** (at 409 nm) decreases with increasing amount of water (Fig. S28, ESI†). In presence of Zn^{2+}, absorbance of **AAS** decreases at 414 nm, and increases at 522 nm with increasing water content (Fig. S29, ESI†). In presence of Zn^{2+} (in methanol), the absorbance of **AAS** is red shifted from 409 nm to 460 nm along with two isosbestic points at 424 nm and 265 nm (Fig. 2).

Plot of absorbance *vs.* concentration of Zn^{2+} have yielded a sigmoidal curve with a linear region up to 10 μM Zn^{2+}

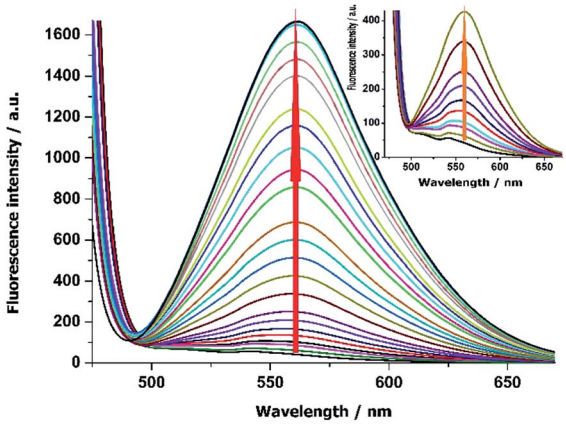

Fig. 1 Changes in the fluorescence spectra of **AAS** (10 μM) upon gradual addition of Zn^{2+} (0.0001, 0.0005, 0.001, 0.005, 0.01, 0.05, 0.1, 0.5, 1.0, 2.0, 3.0, 4.0, 5.0, 6.0, 8.0, 10.0, 15.0, 25.0, 30.0, 40.0, 50.0, and 100.0 μM) in dry methanol. Inset: lower concentration (0.0001 μM to 1.0 μM).

(Fig. S30, ESI†). The naked eye yellow colour changes are observed consistently upon addition of Zn^{2+} (Fig. S31, ESI†). On the other hand, in aqueous methanol, the band at 409 nm gradually decreases with the appearance of three new bands at 348 nm, 482 nm and 517 nm respectively due to complexation between **AAS** and Zn^{2+} (Fig. S32, ESI†). Corresponding naked eye colour changes due to gradual addition of Zn^{2+} and time dependent colour changes of the **AAS–Zn^{2+}** complex under UV-lamp are shown in Fig. 3.

3.2 Effects of pH on spectroscopic properties of AAS

The emission intensities of free **AAS** and **AAS–Zn^{2+}** systems are almost equal at lower pH (up to pH 4.0) (Fig. S14, ESI†). Free **AAS** shows slight fluorescence enhancement above pH 4.0 and gradually decreases above pH 6.0. Whereas the emission intensity of **AAS–Zn^{2+}** system gradually increases with pH, reaching maximum in the pH range 7.0 to 9.0 and finally

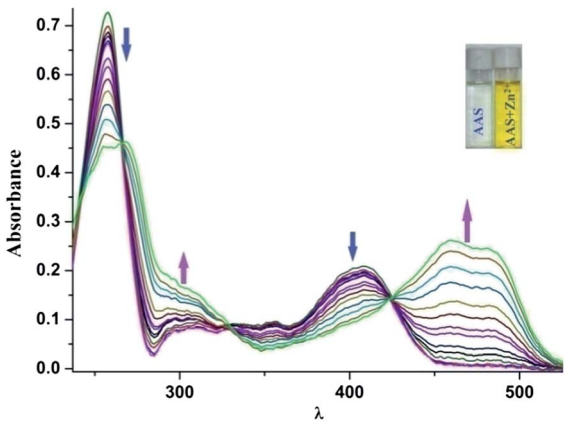

Fig. 2 Changes in the absorbance of **AAS** (10 μM) upon gradual addition of Zn^{2+} in dry methanol (free **AAS**, 0.0005, 0.005, 0.05, 0.5, 1.0, 3.0, 5.0, 8.0, 10.0, 15.0, 30.0, 40.0, 50.0, and 100.0 μM Zn^{2+}, from bottom to top).

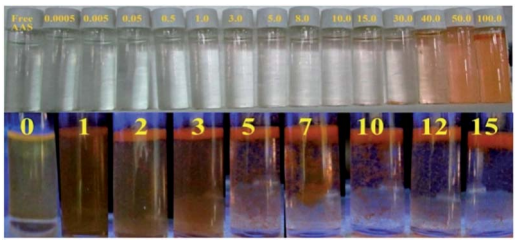

Fig. 3 Naked eye color change of **AAS** (10 μM) in water, HEPES buffer (0.1 M, pH 7.4) upon gradual addition of Zn^{2+} (μM) at room temperature (top) and formation of red color **AAS–Zn^{2+}** complex as a function of time (min) in water–methanol (97.5 : 2.5, v/v, [Zn^{2+}] = 100 μM, [**AAS**] = 10 μM) under UV-lamp.

decreases above pH 9.0. Probably, at higher pH, precipitation of Zn^{2+} occurs while at lower pH, H^+ competes with Zn^{2+} for binding with **AAS**.

3.3 Determination of the binding constant of the AAS–Zn^{2+} complex

Job's plot (Fig. S23, ESI†) indicates 2 : 1 (**AAS** : Zn^{2+}, mol ratio) stoichiometry of the **AAS–Zn^{2+}** adduct. In dry methanol, the equilibrium binding constant of **AAS** for Zn^{2+} is $3.049 \times 10^5\ M^{-1/2}$ as measured using Benesi–Hildebrand[32] equation (Fig. S24, ESI†).

3.4 Zn^{2+} binding selectivity of AAS

Emission properties of **AAS** with common cations *viz.* Na^+, K^+, Ca^{2+}, Mg^{2+}, Mn^{2+}, Ni^{2+}, Cr^{3+}, Fe^{3+}, Al^{3+}, Zn^{2+}, Cu^{2+}, Co^{2+}, Hg^{2+}, Pb^{2+} and Cd^{2+} have been investigated both in dry methanol (Fig. 4) and HEPES buffered (0.1 M, pH, 7.4) water–methanol (97.5 : 2.5, v/v) media. Fig. 1 reveals that emission intensity of **AAS** significantly enhanced in presence of Zn^{2+}. Colours of **AAS** in presence of different cations under UV light as well as through naked eye are shown in Fig. S15 (ESI†). No significant interferences have been found from common cations as mentioned *supra* (Fig. S16, in ESI†).

Furthermore **AAS** is also highly Zn^{2+} selective in presence of common anions (*viz.* PO_4^{3-}, AsO_4^{3-}, AcO^-, F^-, Cl^-, Br^-, I^-, NO_3^-, NO_2^-, $SO_4^{2-}$and SCN^-) and no anion interference was observed during detection of Zn^{2+} (Fig. S17 and inset of Fig. S17 in ESI†).

3.5 Solid state fluorescence property of AAS–Zn^{2+} complex

The **AAS–Zn^{2+}** adduct have a strong solid state red fluorescence at 605 nm. In dry methanol, the yellow colour **AAS** turns red in presence of high Zn^{2+} concentration (>100 μM) while the same phenomenon is observed in aqueous methanol (water–methanol, 97.5 : 2.5, v/v) at >50 μM Zn^{2+}. In solid state, **AAS** and **AAS–Zn^{2+}** adduct have emissions at 545 nm and 605 nm respectively (Fig. S25, ESI†). Naked eye and UV irradiated colours of solid **AAS** and **AAS–Zn^{2+}** adduct are shown in Fig. S26 (in ESI†). Mortar–pestle grinding of solid **AAS** with traces of Zn^{2+} salt also generates visibly orange colour complex having red fluorescence (Fig. 5).

Thus **AAS** is an excellent ligand for detection of Zn^{2+} in real sample by Mortar–pestle grinding or by a dipstick probe for the detection of Zn^{2+} in water, completely avoiding organic solvents. For this purpose **AAS** was adsorbed on alumina, a slurry of which was coated on a thermoplastic stick as support. Solid state detection of Zn^{2+} also performed also in presence of various common anions (Fig. S27 in ESI†). Thus, **AAS** can be employed as a laboratory indicator for detection of Zn^{2+} in real sample.

3.6 Zn^{2+} binding modes of AAS

Solvent dependent and Zn^{2+} concentration regulated differential interaction between **AAS** and Zn^{2+} is also nicely demonstrated by ^1H NMR titration in DMSO-d_6 (Fig. 6) which reveals 0.02 ppm (δ = 11.531 to 11.552) downfield shift of –NH of acridone, 0.016 ppm downfield shift of –OH and 0.034 ppm upfield shift of imine proton upon addition of 2.5 equivalent Zn^{2+} to **AAS** indicating interaction of these donor sites with Zn^{2+} leading to chelation enhanced fluorescence (CHEF). Upon

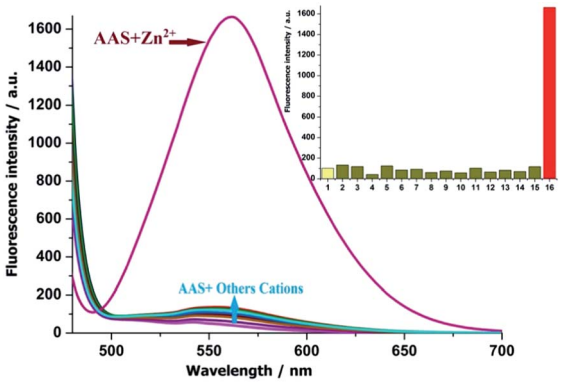

Fig. 4 Fluorescence spectra of **AAS** (10 μM) in presence of common cations (100 μM) in dry methanol: (1) free **AAS**, (2) Na^+, (3) K^+, (4) Ca^{2+}, (5) Mg^{2+}, (6) Mn^{2+}, (7) Ni^{2+}, (8) Cr^{3+}, (9) Fe^{3+}, (10) Al^{3+}, (11) Cu^{2+}, (12) Co^{2+}, (13) Hg^{2+}, (14) Pb^{2+}, (15) Cd^{2+} and (16) Zn^{2+}; λ_{ex} = 445 nm. Inset: respective emission intensities.

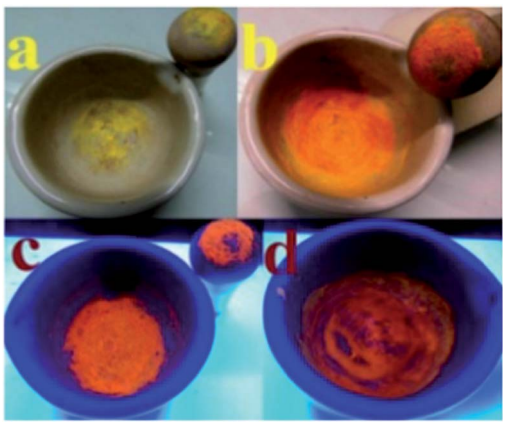

Fig. 5 (a) Naked eye colour of free **AAS** and (b) after mortar–pestle grinding with Zn^{2+} in presence of other common cations, (c) colour of **AAS** in presence of Zn^{2+} under UV light and (d) colour of **AAS** under UV light with **Zn^{2+}** in presence of other common cations. **AAS** shows slight yellowish-green colour under UV light (Fig. S26(c) in ESI†).

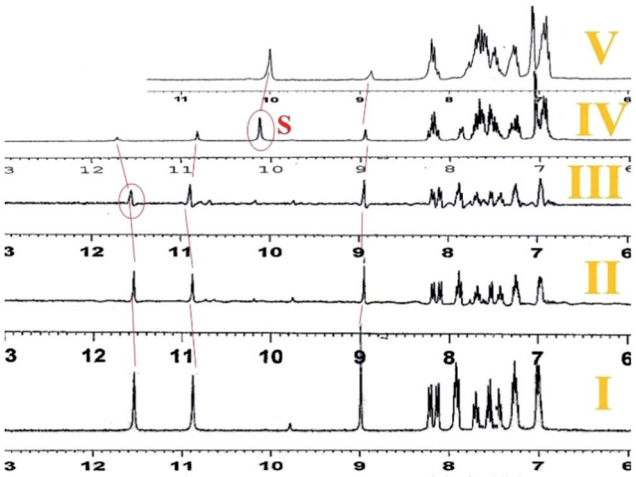

Fig. 6 ^{1}H NMR spectral changes of **AAS** after interacting with Zn^{2+}: (I) free **AAS**; (II) **AAS** + 0.5 equivalent Zn^{2+}; (III) **AAS** + 2.5 equivalent Zn^{2+}; (IV) **AAS** + 2.5 equivalent Zn^{2+} + 0.1 mL D_2O; (V) **AAS** + 2.5 equivalent Zn^{2+} + 0.3 mL D_2O. ^{1}H NMRs are recorded in 0.5 mL DMSO-d_6. "S" is the new 'NH' proton.

addition of water to the **Zn^{2+}–AAS** complex or at higher Zn^{2+} concentration, the keto form predominates, responsible for red shift of the emission band from 560 nm (dry methanol) to 565 nm (aqueous methanol). Addition of 0.1 mL D_2O to 0.5 mL DMSO-d_6 solution of **AAS–Zn^{2+}** adduct results a new peak at 10.12 ppm, assigned to a new –NH proton(s) arising due to keto–enol tautomerism. Thus the imine bond is lost leading to free rotation feasible. The –NH proton of acridone further downfield shifted to 11.72 ppm. Further addition of 0.2 mL D_2O, complete the appearance of the new proton. ^{1}H NMR of the isolated red complex (DMSO-d_6, in spite of its very poor solubility) shows only one –NH proton at 9.21 ppm (Fig. S33, ESI†), demonstrating that –NH proton of acridone also takes part into keto–enol tautomerism (acridine). These type of molecules have the molecular structure to give ESIPT.[33] Mass spectrum also support the adduct formation involving two **AAS** units with one Zn^{2+} in dry methanol. In presence of water, one H_2O acts as a linker between two **AAS–Zn^{2+}** units (Fig. S34 and S35 respectively, ESI†), which support the polymer formation. Thermogravimetric analyses (TGA) of **AAS** and **AAS–Zn^{2+}** complex

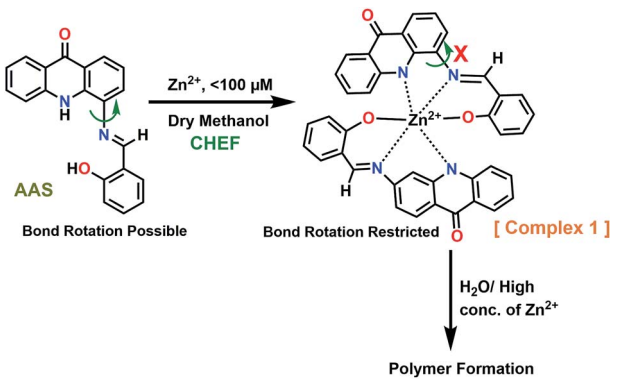

Fig. 7 Plausible binding mechanism of **AAS** with Zn^{2+}.

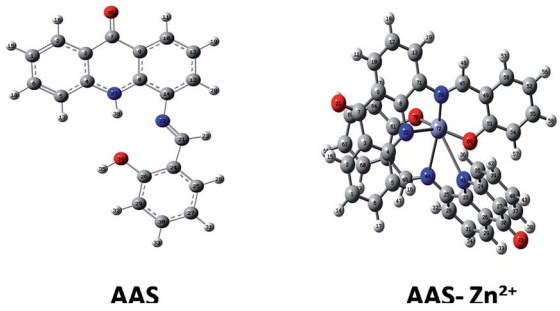

Fig. 8 Energy optimised structures of **AAS** and **AAS–Zn^{2+}**.

(Fig. S37 and S38, ESI†) are distinctly different. Loss of H_2O between 102.8 °C and 168.0 °C corresponding to ~4.64% weight loss clearly establishes our proposed **AAS–Zn^{2+}** adduct (Fig. S38, ESI†). Since EDTA is a good Zn^{2+} chelator, decomplexation of the red solid would be expected upon washing with EDTA solution but the red solid remain unchanged by EDTA solution. Thus we expected the red solid may be a polymeric complex. The plausible binding mechanism of **AAS** with Zn^{2+} has been shown in Fig. 7. **AAS** is weak emitter due to ICT process. Addition of Zn^{2+} in dry methanol inhibits ICT to produce CHEF. Upon addition of water to the system, an intermediate state is observed where imine bond breaks and imine N centre gets protonated. When amount of water is relatively high, then complete proton transfer from –OH to imine –N centre occurs[34] (Fig. S39, ESI†). At higher Zn^{2+} or water concentration, deprotonation of OH leading to formation of C=O occurs and subsequently the red complex polymer forms (Fig. 7). Fig. S33 (ESI†) reveals that the polymeric **AAS–Zn^{2+}** complex have no –OH or acridone–NH protons. So, it is electrically neutral and gets precipitated in polar solvent. Life time measurement experiment of **AAS**, [**AAS–Zn^{2+}**] and [**AAS–Zn^{2+}–Water**] with addition of water also supports the involvement of ESIPT process (Fig. S40 in ESI†).

3.7 DFT calculation and theoretical study

DFT calculations are performed to better understand the possible binding modes of **AAS** with Zn^{2+}. The optimized geometries of **AAS** (Fig. 8) and **AAS–Zn^{2+}** adduct (Fig. 9) are

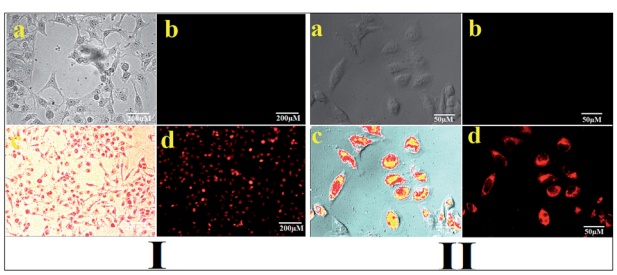

Fig. 9 Fluorescence microscope images of (I) human breast cancer MCF7 cell and (II) *HeLa* cell: (a) and (b) are bright field and fluorescence images of cells after 30 min incubation with Zn^{2+} (50 μM); (c) and (d) are bright field and fluorescence images of Zn^{2+} (50 μM) incubated cells after 2 h treatment with **AAS** (10 μM).

generated using 3-21G/B3LYP basis sets respectively of Gaussian 09 software.[35] In free **AAS** the HOMO lies in acridone ring and the LUMO spreads over in the salicylaldehyde imine part (Fig. S41†). On complexation the energy of individual HOMO and LUMO decreases and the energy gap between the highest occupied molecular orbital (HOMO) and lowest unoccupied molecular orbital (LUMO) also decreases, thus there is an increase in the stability of the whole system (Fig. S41†). Hence, the observed red shift in the absorption spectra of **AAS–Zn^{2+}** can be explained in the terms of decreased band gap of HOMO and LUMO.

3.8 Cell culture study

To further demonstrate the practical application of the probe, we carried out experiments in living cells (detail in ESI†). **AAS** is very efficient to detect intracellular Zn^{2+} in human breast cancer cell, MCF7 and *HeLa* cells under normal and fluorescence microscope (Fig. 9). Incubation of cells with Zn^{2+} (50 μM) for 30 min. at 37 °C was followed by the addition of **AAS** (10 μM) after washing three times with media and then was incubated further for another 2 h. The enhancement of fluorescence was observed (Fig. 9). The results suggest that **AAS** can penetrate the cell membrane and can be used for imaging of Zn^{2+} in living cells. Furthermore, we have investigated the cell permeability of **AAS** in presence and absence of an intracellular zinc chelator **TPEN**, the results shows that **AAS** is cell permeable and can be used to detect intracellular zinc ion concentration (Fig. S42, in ESI†). In presence of **TPEN**, the fluorescence of [**AAS–Zn^{2+}**] completely diminished due to the unavailability of Zn^{2+} ion in cells.

3.9 Cytotoxicity of AAS

Further, the cytotoxicity of **AAS** on MCF7 and *HeLa* cells was determined by a conventional MTT assay (details in ESI, Fig. S43†), which revealed that, upon exposure to a 10 μM concentration of **AAS** (a concentration that was comparable to that used for confocal imaging studies; Fig. 8) for 12 h, ~90% of the cells remained viable. This nullified the possibility of any significant cytotoxic influence of the reagent **AAS** on *HeLa* cells. Therefore, it may be concluded that **AAS** could be used as a viable chemosensor for Zn^{2+} in biological samples.

4. Conclusion

Thus, an acridone based probe generates solid state red fluorescence in presence of trace level Zn^{2+} having naked eye orange color in presence of all the other cation and anion including biologically important ones. Interference free detection of Zn^{2+} in real sample and live cells is possible. The polymeric red emitting **AAS–Zn^{2+}** complex may be useful as optoelectronic materials.

Acknowledgements

Authors acknowledge Dr R. Banerjee (IICT, Hyderabad) for cell imaging studies. A. Ghosh and S. Mandal are thankful to UGC, New Delhi and A. Sahana to CSIR, New Delhi for providing fellowships. S. Adhikari acknowledges the SERB-DST (project no. SR/S1/OC-101/2012) for financial support.

Notes and references

1 R. S. MacDonald, *J. Nutr.*, 2000, **130**, 1500S–1508S.
2 R. B. Franklin and L. C. Costello, *J. Cell. Biochem.*, 2009, **106**, 750–757.
3 E. L. Que, D. W. Domsille and C. J. Chang, *Chem. Rev.*, 2008, **108**, 1517–1549.
4 E. Cohen-Kfir, W. Lee, S. Eskandari and N. Nelson, *Proc. Natl. Acad. Sci. U. S. A.*, 2005, **102**, 6154–6159.
5 V. Petkovic, M. C. Miletta, A. Eblé, D. I. Iliev, G. Binder, C. E. Flück and P. E. Mullis, *Endocrinology*, 2013, **154**, 4215–4225.
6 W. Swardfager, N. Herrmann, G. Mazereeuw, K. Goldberger, T. Harimoto and K. L. Lanctôt, *Biol. Psychiatry*, 2013, **74**, 872–878.
7 S. J. Lee and J. Y. Koh, *Mol. Brain*, 2010, **3**, 30.
8 L. C. Costello, Y. Liu, J. Zou and R. B. Franklin, *J. Biol. Chem.*, 1999, **274**, 17499–17504.
9 S. M. Henshall, D. E. H. Afar, K. K. Rasiah, L. G. Horvath, K. Gish, I. Caras, V. Ramakrishnan, M. Wong, U. Jeffry and J. G. Kench, *Oncogene*, 2003, **22**, 6005–6012.
10 L. C. Costello, R. B. Franklin, P. Feng, M. Tan and O. Bagasra, *Cancer, Causes Control*, 2005, **16**, 901–915.
11 E. Ho and Y. Song, *Curr. Opin. Clin. Nutr. Metab. Care*, 2009, **12**, 640–645.
12 A. S. Om and K. W. Chung, *J. Nutr.*, 1996, **126**, 842–848.
13 M. F. Leitzmann, M. J. Stampfer, K. Wu, G. A. Colditz, W. C. Willett and E. L. Giovannucci, *J. Natl. Cancer Inst.*, 2003, **95**, 1004–1007.
14 S. Y. Park, L. R. Wilkens, J. S. Morris, B. E. Henderson and L. N. Kolonel, *Prostate*, 2013, **73**, 261–266.
15 J. J. Hwang, H. N. Kim, J. Kim, D. H. Cho, M. J. Kim, Y. S. Kim, Y. Kim, S. J. Park and J. Y. Koh, *BioMetals*, 2010, **23**, 997–1013.
16 A. Sahana, A. Banerjee, S. Lohar, S. Panja, S. K. Mukhopadhyay, J. S. Matalobos and D. Das, *Chem. Commun.*, 2013, **49**, 7231–7233.
17 T. Hirano, K. Kikuchi, Y. Urano, T. Higuchi and T. Nagano, *J. Am. Chem. Soc.*, 2000, **122**, 12399–12400.
18 R. Weissleder, *Nat. Biotechnol.*, 2001, **19**, 316–317.
19 L. Yuan, W. Lin, K. Zheng, L. He and W. Huang, *Chem. Soc. Rev.*, 2013, **42**, 622–661.
20 S. C. Burdette, G. K. Walkup, B. Spingler, R. Y. Tsien and S. J. Lippard, *J. Am. Chem. Soc.*, 2001, **123**, 7831–7841.
21 Z. Xu, X. Liu, J. Panb and D. R. Spring, *Chem. Commun.*, 2012, **48**, 4764–4766.
22 L. Xue, C. Liu and H. Jiang, *Org. Lett.*, 2009, **11**, 1655–1658.
23 S. Goswamia, S. Das, K. Aich, D. Sarkar and T. K. Mondal, *Tetrahedron Lett.*, 2013, **54**, 6892–6896.
24 S. Goswami, A. K. Das, K. Aich, A. Manna, S. Maity, K. Khanra and N. Bhattacharyya, *Analyst*, 2013, **138**, 4593–4598.
25 S. Goswami, A. K. Das, B. Pakhira, S. B. Roy, A. K. Maity, P. Saha and S. Sarkar, *Dalton Trans.*, 2014, **43**, 12689–12697.

26 Y. Xu, L. Xiao, S. Sun, Z. Pei, Y. Pei and Y. Pang, *Chem. Commun.*, 2014, **50**, 7514–7516.
27 C. Pal, M. K. Kundu, U. Bandyopadhyay and S. Adhikari, *Bioorg. Med. Chem. Lett.*, 2011, **21**, 3563–3567.
28 S. Fukuzumi and K. Ohkubo, *J. Am. Chem. Soc.*, 2002, **124**, 10270–10271.
29 J. A. Smith, R. M. West and M. Allen, *J. Fluoresc.*, 2004, **14**, 151–171.
30 D. Karak, A. Banerjee, A. Sahana, S. Guha, S. Lohar, S. Adhikari and D. Das, *J. Hazard. Mater.*, 2011, **188**, 274–280.
31 A. I. Vogel, *A text book of Macro and Semimicro Qualitative Inorganic Analysis*, 4th edn, 1953.
32 H. A. Benesi and J. H. Hildebrand, *J. Am. Chem. Soc.*, 1949, **71**, 2703–2707.
33 G. Liu, B. Li and J. Shao, *J. Inclusion Phenom. Macrocyclic Chem.*, 2014, **78**, 97–102.
34 S. Guha, S. Lohar, A. Sahana, A. Banerjee, D. A. Safin, M. G. Babashkina, M. P. Mitoraj, M. Bolte, Y. Garcia, S. K. Mukhopadhyay and D. Das, *Dalton Trans.*, 2013, **42**, 10198–10207.
35 M. Frisch, G. Trucks, H. Schlegel, G. Scuseria, M. Robb and J. Cheeseman, *et al.*, *Gaussian 09, revision A.01*, Gaussian, Inc, Wallingford, CT, 2009.

